

Simplifying BRDF Acquisition

SHUBHAM CHITNIS,¹ ADITYA SOLE,² SHARAT CHANDRAN¹

¹ Department of Computer Science and Engineering, Indian Institute of Technology Bombay, India 400076

² Colourlab, Department of Computer Science, Norwegian University of Science and Technology (NTNU),

Gjøvik, 2815, Norway

¹shubham.chitnis,sharat@iitb.ac.in

²aditya.sole@ntnu.no

Abstract: Non-diffuse materials like metallic inks, varnish coatings, and paints are widely used (for example, on e-commerce boxes). Synthetic rendering is a significant pre-processing step in the fulfillment process. An important attribute of this is the bidirectional reflection distribution function (BRDF). Current methods of capturing spectral BRDF for complex material are tedious, energy-inefficient, expensive, and sometimes error-prone.

In this paper, we focus on in-plane measurements, a tiny subset of the entire gamut of possible measurements for isotropic materials considerably simplifying the acquisition process. We demonstrate that, by using a parametric representation in the RGB space, substantially small datasets can be representative of the optical properties of many commonly seen materials while maintaining visual fidelity.

Conceding that RGB space may be too restrictive in some applications, we also consider in this paper the acquisition of 31 wavelengths. Here, we suggest the use of a multilayer perceptron as a means to provide compact material representations in the much more vast spectral space. Our neural-based scenario suggests the acquisition of far fewer measurements while maintaining significant saliency.

© 2024 Optical Society of America under the terms of the [OSA Open Access Publishing Agreement](#)

1. Introduction

Materials with complex optical properties can produce captivating effects in various manufactured products, such as paints and speciality coatings. For instance, they enhance the packaging of cosmetics, alcoholic beverages, and fragrances. These products are produced using different printing techniques and necessitate visual renderings for customer validation and meticulous quality control before production.

Depending on the illumination and reflected directions, the appearance of these materials can change in terms of perceived lightness, or even color (termed goniochromatism, or iridescence). This change is due to the change in the amount and nature of light reflected (spectrally) from the material in a given direction. Figure 1 shows the spectral BRDF of a goniochromatic packaging print material that we use in this paper. Measurement of, or modeling, the properties of such materials therefore is paramount.

The surface reflectance of these opaque materials is classically modeled using the bidirectional reflectance distribution function (BRDF) defined by Nicodemus et al. [1] and given in Equation 1.

$$f_\lambda(\mathbf{I}, \mathbf{v}) = \frac{dL_r(\mathbf{v})}{dE_i(\mathbf{I})} = \frac{dL_r(\mathbf{v})}{L_i(\mathbf{I}) \cos \theta_i d\omega_i} \quad (1)$$

In Equation 1, \mathbf{I} and \mathbf{v} are incident and reflected direction unit vectors, E_i is incident spectral irradiance, L_i is incident spectral radiance (flux per unit projected area, per unit solid angle (ω_i)) at the incoming angle θ_i , L_r is the reflected spectral radiance in the direction v out of any of the infinite reflected directions of interest, and d is the differential. The unit of a BRDF is inverse steradian (1/sr) and an explicit reference is made to the wavelength of interest, λ .

From the perspective of rendering, for many decades, the BRDF was modeled simply as a

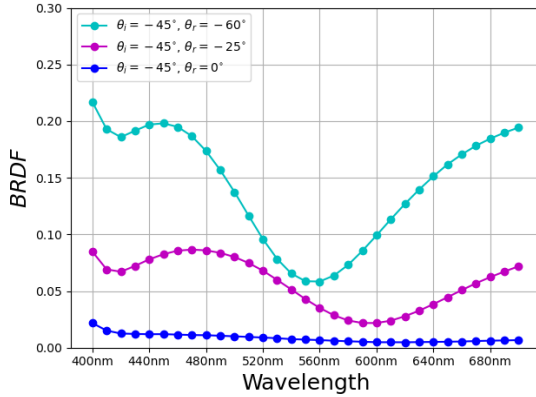


Fig. 1. Goniochromatic materials have complex appearances. For the same incident angle of illumination (-45°), depending on the reflected angle (-60° , -25° and 0°), the measured spectral BRDF can be vastly different (note the trough in the -25° case compared to the -60°). Saris and kurtas seen in social contexts in India exhibit this effect.

44 constant, and this was reasonable for early applications. With increased sophistication, accurate
 45 BRDF values for a variety of materials are needed. Multi-angle spectrophotometers and goniophotometers
 46 can measure the bidirectional reflectance from the material surface [2] and use these measurements for modelling the BRDF. Nonetheless, BRDF measurements – the fodder
 47 for appearance modeling – take a considerable amount of time to be obtained. For instance, the
 48 measurement times, even with the state-of-the-art approach, can take “2-3 days for anisotropic
 49 materials” [3]. This has led to the use of compact parametric analytical material representations.

50 Parametric models [4] can be compact phenomenological or physically based, and application-specific.
 51 These models circumvent some of the issues faced by traditional lookup table methods
 52 that are heavy (“big data”) and highly material-specific. The “ABC” parametric model [5] defined
 53 in Equation 7 in Appendix A and used in this paper is based on the well-established micro-facet
 54 Cook-Torrance model [6]. This model takes into account glossy surfaces and is based on the
 55 Rayleigh-Rice light scattering theory and the related micro-facet theory. Data-driven approaches
 56 are then used to fit all the previously collected “big” data into succinct parameters.

58 1.1. Objective A: In-plane fitting

59 Existing works, however, fail to ask the question of *how little data* is sufficient for building
 60 a parametric model to learn the underlying BRDF trends. Instead of working over the entire
 61 hemisphere centered around a point on the material, one can consider in-plane measurements
 62 that are restricted to moving the source and the sensor in a single plane. Since in-plane data
 63 collection is less time-intensive, in this paper, our first objective is exploring the use of in-plane
 64 bidirectional reflectance measurements to model material BRDF of four real-life packaging print
 65 materials in the RGB rendering space. Although rendering is restricted to RGB, these materials
 66 exhibit complex optical properties such as non-diffuse and goniochromatic (Figure 1) reflection.

67 1.2. Objective B: Spectral Measurements

68 An obvious pitfall of using tristimulus RGB to validate in-plane measurements is the shrinking
 69 of the vast spectral data from multiple wavelengths to three principal ones. Furthermore, even
 70 restricting the number of wavelengths to meaningful practical levels, we find that the amount
 71 of BRDF can be quite large for any one single wavelength based on the choice of incident and

72 reflected directions.

73 With the success of deep learning methods, one can either directly regress the final RGB-
74 based appearance from measurements without generating intermediate representation, or, more
75 recently [7, 8], generate latent representations that help in the final neural generation of the
76 appearance. These methods take the big data and exploit them in novel ways. Being more
77 expressive, neural networks possess the ability to represent a wide range of materials and thus
78 are impervious to model-specific representations.

79 However, as discussed in Section 4.1 none of the existing ANN-based methods actually
80 **produce** spectral measurements. Instead, the goal is always the downstream task of processing in
81 the tristimulus domain without explicitly addressing the problem of creating multi-spectral data.
82 A second objective of this paper is to turn to, in effect, software measurements using artificial
83 neural networks (ANN) to reduce the acquisition cost.

84 **1.3. Contributions**

85 For both of the above objectives, our goal is to simplify the acquisition of BRDF values, and not
86 the downstream tasks such as BRDF editing. Our contributions in this paper can be summarized
87 as follows:

- 88 1. We posit the use of in-plane measurements to represent the *appearance* of diffuse *and*
89 non-diffuse packaging print materials. This has not been considered in the literature. We
90 show that in-plane measurements besides being swift to acquire are sufficient for *visual*
91 *rendering* and we *quantitatively* compare and outperform the state of the art on publicly
92 available data.
- 93 2. We present a multi-layer perceptron network to *output spectral* BRDF of non-diffuse and
94 (“difficult”) goniochromatic packaging print materials. We emphasize that unlike other
95 work, we output multispectral BRDF values while reducing the acquisition cost, and do
96 not restrict ourselves to rendering.
- 97 3. We provide access to the code and spectral measurement data to the scientific community
98 for further research and to reproduce the results.

99 For Objective B, and for the sake of ground truth, we perform time consuming measurements
100 (31 wavelengths, and a total of 900 incident-reflection angle pairs) on four off-the-shelf packaging
101 materials and contrast our software-driven acquisition against the full measurement dataset for a
102 “what-if” comparison. For Objective A, we fortify our claims with five representative materials
103 from the publicly available MERL dataset [9] (in addition to results for our own measurements).
104 The MERL materials have well established ground truths and thus are amenable to evaluate the
105 accuracy of our results.

106 **2. Data Collection**

107 We describe the two types of datasets that are used to validate our methods. First, we briefly
108 discuss the publically available dataset, and later describe how we laboriously measured our
109 packaging materials. Measurement of BRDF for materials with complex reflectance properties
110 can be challenging [3, 10, 11]. The high dimensionality function with essentially infinite angles
111 can be expensive in terms of time and physical setup required for measurement. A variety of
112 measurement setup designs and methods have been proposed (see [4]). We discuss our method
113 in Section 2.2.

114 **2.1. Public Data**

115 The MERL database [9] from the early 2000s is a classic source of the BRDF for ~ 100 isotropic
116 materials. The acquisition setup differs from ours (see Section 2.2) in that they use a *camera*-based

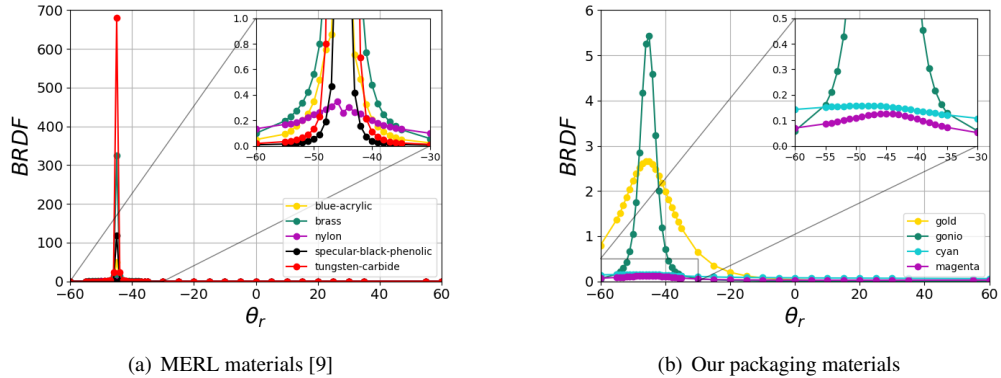


Fig. 2. Bidirectional reflectance (f) measured at 560nm for an incident angle $\theta_i = -45^\circ$ and various reflected angles θ_r .

turntable arrangement to capture multiple high-dynamic range pictures of their materials. Using spherical samples allows them to treat every pixel as a measurement. Data post-processing follows, which involves outlier removal and smoothing to get rid of measurement noise. According to the authors, for every material, 20-80 million samples are captured over a three-hour time period. This data, however, compresses the varied frequency dependency into three RGB values. As noted in [3], this requires an awkward heuristic conversion to be usable in spectral renderers.

Five materials are used to evaluate our method of using the in-plane measurement dataset against the full measurements in the MERL dataset. These five MERL materials were chosen to cover a wide range of reflectance properties. This variation is apparent in Figure 2(a), where we show the reflectance properties of the chosen MERL materials. For reference, we also show (Figure 2(b)) the reflectance properties of our packaging print materials (Section 2.2).

128 2.2. Packaging-Material Data

129 In this work, we provide data for four packaging print materials named *CN*, *MaG*, *Gold*, and
 130 *Gonio* that are commonly used in the print and packaging industry for decoration and bottle
 131 packaging. *CN* (looking like cyan), and *MaG* (looking like magenta) reflect the incident light
 132 diffusely, whereas *Gold* and *Gonio* are non-diffuse. *Gonio* is a goniochromatic material that
 133 showed a shift in the chromaticity with the change in the reflected direction as shown in Figure 1.
 134 *Gold* (gold in color) is a thin metallic cardboard commonly used for decoration and bottle
 135 packaging.

136 The BRDF for the packaging print materials were measured using Murakami's GCMS-3B
 137 goniospectrophotometric color measurement system, henceforth referred to as GCMS. Figure 3(a)
 138 shows a conceptual diagram. An ANSI standard Munsell white N9 sheet was measured along
 139 with the packaging print materials and used as reference white to estimate the bidirectional
 140 reflectance factor (see Appendix B) at the material surface. The irradiance at the material surface
 141 was estimated using a point light source having a spectral power distribution (SPD) as shown in
 142 Figure 3(b). GCMS records the spectral radiance factor (390nm – 730nm at 10nm intervals) at
 143 anormal incident (θ_i) and reflection (θ_r) angles in the range of $+80^\circ$ to -80° at 5° intervals. It
 144 uses a tungsten halogen light bulb to illuminate the materials and a silicon photo-diode array as
 145 a detector to detect the reflected light. The material to be measured rotates between anormal
 146 angles $\pm 80^\circ$ with respect to the incident light source that is normal to the material surface. The
 147 instrument provides the radiance factor at the material surface as an output after correcting for
 148 the change in illumination and reflected area due to rotation. We calculate the bidirectional

reflectance at the material surface using Equation 13, Appendix B and the Munsell white N9 sheet with reflectivity of 79%. For the experiments discussed in this paper, GCMS performs in-plane measurements that take approximately 3 hours to measure a single material.

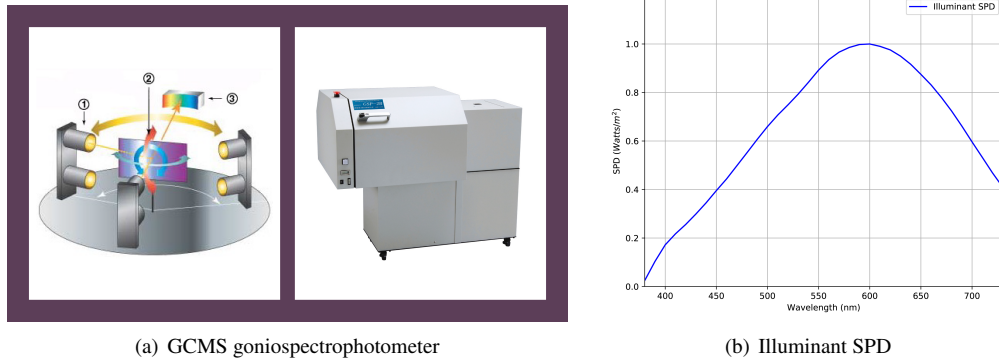


Fig. 3. (Left) The GCMS goniospectrophotometer prototype [<https://www.merl.co.jp>]. (Right) Spectral power distribution (SPD) of the point light source.

Considering the documented measurement uncertainty at grazing directions for the GCMS, measurements recorded outside the range of $+60^\circ$ to -60° for both the illumination and reflected directions were not used in fitting the material BRDF for the packaging print materials. The measurement data obtained from the GCMS and used in this study therefore consisted of 31 wavelengths (400nm - 700nm at 10nm interval) and a total of 900 incident-reflection angle pairs (for 25 unique incident angles at an interval of 5°).

3. Objective A: In-plane Parametric Fitting

Traditionally, if complete hemispherical BRDF measurements are available, a lookup table can be created with the available measurements, and intermediate values are interpolated for BRDF evaluation. With only the in-plane measurement data from the GCMS, it is crucial to be able to estimate out-of-plane BRDF measurement data for 3D renderings. We turn to the ABC analytical model which might offer a viable option for model fitting since there is generally no restriction on the number of materials used. This hypothesis is verified in Section 3.3.

3.1. GCMS Fitting

However, existing parametric representations are in the RGB space [5, 6, 12]. This does not pose a problem for the MERL data which is in RGB space. In contrast, in this paper, the BRDF measurements obtained (see Section 2.2) from the GCMS are spectral. This compels us to perform a compression step which will project all the 31 spectral wavelengths into tristimulus data. One can use the CIE standard observer matching functions (\bar{x}_λ , \bar{y}_λ and \bar{z}_λ) for this purpose. The dot product across the 31 wavelengths, as shown in Equation 2 was used to convert the spectral BRDF measurements obtained from the GCMS into tristimulus data (X_{GCMS} , Y_{GCMS} , Z_{GCMS}).

$$X_{\text{GCMS}} = k \sum_{\lambda=400\text{nm}}^{700\text{nm}} f_\lambda E_\lambda(i) \bar{x}_\lambda$$

$$k = \frac{100}{\sum_{\lambda=400\text{nm}}^{700\text{nm}} E_\lambda(i) \bar{y}_\lambda} \quad (2)$$

174 In Equation 2, k is the normalizing factor, f the measured BRDF value, and $E(i)$ is an estimate
 175 of the illuminant spectral power distribution. Equivalent equations for Y_{GCMS} and Z_{GCMS} are
 176 used with \bar{y} and \bar{z} respectively. The tristimulus values are then converted [13] to the RGB space.

177 **3.1.1. Optimization**

178 Consider the nine parameters, $k_{d_{\text{rgb}}}$, A_{rgb} , B , C (implicitly in S), and η (implicitly in F) present
 179 in the parametric model reproduced from Eq. 7 in Appendix A.

$$f(\mathbf{l}, \mathbf{v}) = \frac{k_{d_{\text{rgb}}}}{\pi} + \frac{F(\theta_h)G(\mathbf{n} \cdot \mathbf{l}, \mathbf{n} \cdot \mathbf{v})S_{\text{rgb}}(\sqrt{1 - (\mathbf{n} \cdot \mathbf{h})})}{(\mathbf{n} \cdot \mathbf{l})(\mathbf{n} \cdot \mathbf{v})} \quad (3)$$

180 Here, $k_{d_{\text{rgb}}}$ is the channel-wise diffuse component albedo, and S_{rgb} is the modified ABC
 181 distribution with parameter A being used as a channel-wise scaling parameter. The general idea
 182 is that if we know (or guess) these parameters we can compute the BRDF from Equation 3 and
 183 thus compare, with a suitable cost-function, the measured values.

184 Reviewing the work from [5, 12, 14], the channel-wise micro-facet ABC model was optimised
 185 using Equation 4 as the cost function. In Equation 4, f_{mea} is the measured material BRDF, f_{pred}
 186 is the material BRDF estimated by the fitted parametric model. θ_i and θ_r are the incident and
 187 reflected directions in degrees.

$$\begin{aligned} L_{\text{cus}} &= \frac{1}{N} \sum_{n=1}^N (g_{\text{mea}} - g_{\text{pred}})^2 \sin \theta_r \\ g_{\text{mea}} &= \ln(1 + \cos \theta_i f_{\text{mea}}) \\ g_{\text{pred}} &= \ln(1 + \cos \theta_i f_{\text{pred}}) \end{aligned} \quad (4)$$

190 The logarithmic term has experimentally been shown to give more visually accurate results.

191 **3.2. Fitting Publicly-available Data**

192 As mentioned in the opening, there is a difference between the publicly-available MERL data
 193 and the GCMS data. MERL data is four-dimensional consisting of two polar and azimuthal
 194 angles each for incident and reflected directions. Therefore, we need to choose the plane for
 195 in-plane fitting data. For consistency with GCMS, we keep the same polar angles, and we set the
 196 incident azimuthal angle corresponding to the equatorial angle 0° . In querying the database, we
 197 clamp the reflected directions to have azimuthal angles as either 0° or 180° forming a plane. It
 198 should be noted that we could very well have picked any other incident azimuthal angle since
 199 movement across the azimuthal direction has no effect on isotropic materials provided that the
 200 angle difference stays 180° .

201 For fitting, we follow the pipeline outlined by Low et. al. [5] to optimise for the nine parameters
 202 using the cost function given in Equation 4.

203 **3.3. Objective A: Results**

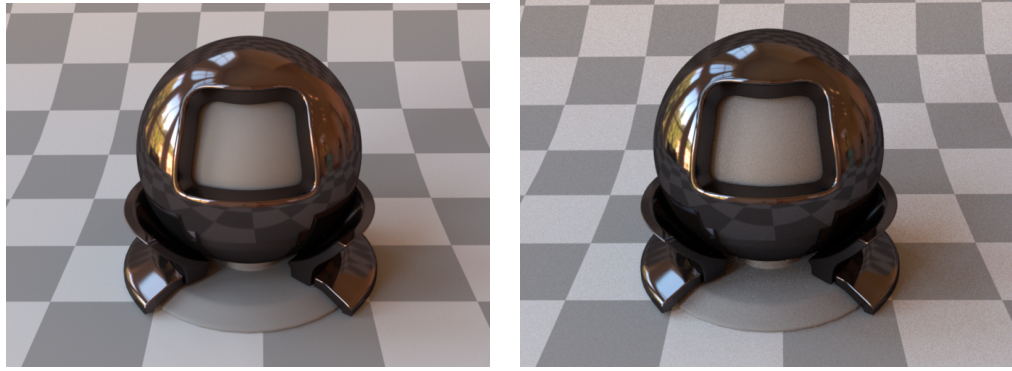
204 For the MERL materials, we limit their measurements by considering the angles in Table 1. This
 205 corresponds directly to the angles measured in Section 2.2. Optimising ABC model parameters
 206 on this data allows us to compare its subsequent renderings with the full gamut of MERL
 207 measurements. This should give a good sense of the applicability and repeatability of in-plane
 208 measurements for the public data 3D rendering. It should be noted that with this dataset, we are
 209 only considering a total of 900 measurements, as opposed to the [5] 28,800 samples per incident
 210 angle (which is approximately 230400 samples (i.e., 256x)).

211 We show three types of results

Dataset	θ_i interval	θ_r interval: Diffuse	θ_r interval: Glossy
DS1	5°	5°	1°

Table 1. Angle intervals used for the in-plane subset of MERL. Both θ_i and θ_r range from -60° to 60° .

- 212 1. Rendering results. We used a Mitsuba [15] plugin for the ABC distribution to produce
 213 renderings of a material preview scene. These are 64 samples per pixel renderings with
 214 lighting provided through an environmental map.



(a) Tungsten, [5]

(b) Tungsten, In-plane only, this paper.

Fig. 4. Scene renderings for visual comparison. Our first result is that rendering with in-plane data (900 samples, right) viewed in isolation is excellent. Further, when viewed comparatively, the results are almost indistinguishable from the one in [5] (230400 samples, left).

215 We show results for the *TungstenCarbide* MERL material¹ in Figure 4. It is clear that
 216 the results are visually indistinguishable. This is remarkable, given that Low et al. use
 217 substantially more data (256x). For completeness, we also show rendering results for new
 218 measurements in this paper of the *Gonio* and *Gold* packaging print materials in Figure 5.

- 219 2. Visual Plots. Figure 6 shows more objectively our claim. The plots match except for a
 220 scaling factor which is possibly an artifact of the differing optimization procedure. Multiple
 221 incident angles return comparable values. The values are shown only for the red channel,
 222 but similar results are obtained for other channels also (see supplementary material for all
 223 materials and all channels).

224 For completeness, we show (Figure 7) the plots for the new measurement data we collected
 225 (Section 2.2).

- 226 3. While the above two results rely on visual inspection, a better sense can be obtained using
 227 a relative rmse error metric, calculated using Equation 5.

$$L_{\text{rel-rmse}} = \sqrt{\frac{1}{N} \sum_{n=1}^N \left(\frac{f_{\text{pred}} - f_{\text{mea}}}{f_{\text{mea}}} \right)^2} \quad (5)$$

¹We pick this material for no particular reason here. Results for other MERL materials are in the supplementary material.

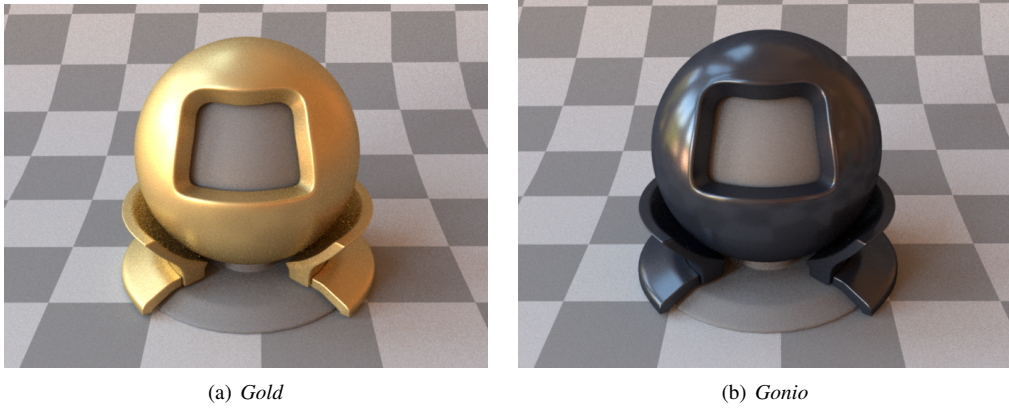
(a) *Gold*(b) *Gonio*

Fig. 5. Scene renderings for our packaging print materials, *Gold* and *Gonio*. These renderings are for in-plane data with only 900 samples.

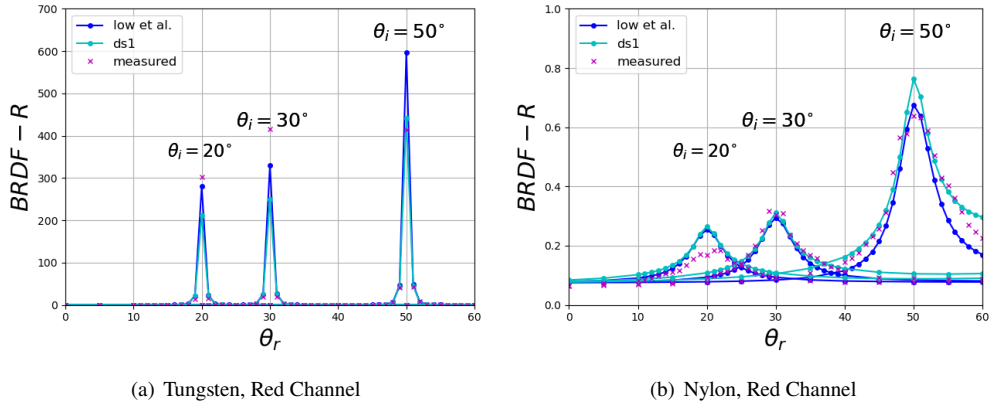


Fig. 6. BRDF of MERL materials calculated with only in-plane data (DS1, this paper) compared to those from [5] (256x data, blue) compared to the much larger complete data (25600x, magenta).

228 Here, f_{mea} and f_{pred} are as defined in Equation 4. For a chosen incident angle, we calculate
 229 this metric for measurements in the glossy region (i.e., where reflected angle approximately
 230 equals the angle of reflection). This is because we expect to see more errors in the glossy
 231 region. Channel-wise relative rmse errors are then averaged to generate the plots in
 232 Figure 8.

233 For completeness, we show (Figure 9) the plots for the data we collected (Section 2.2) and
 234 note that the errors are even lower.

235 Our quantitative results thus justify our claims made earlier in Section 1.3. Ablation studies
 236 are discussed in Appendix C.3. The ablation studies thus justify the claim made in the second
 237 paragraph of the abstract.

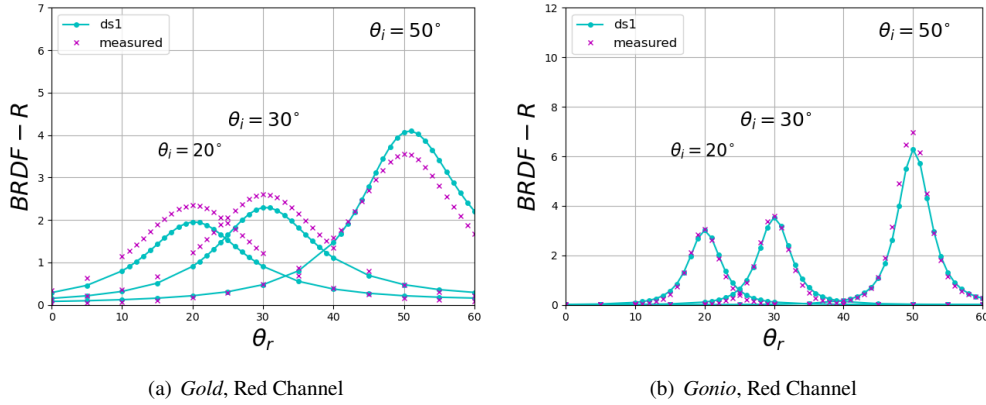


Fig. 7. Contrasting fitted data (DS1 (in-plane measurements only)) with measured BRDF data of two packaging print materials.

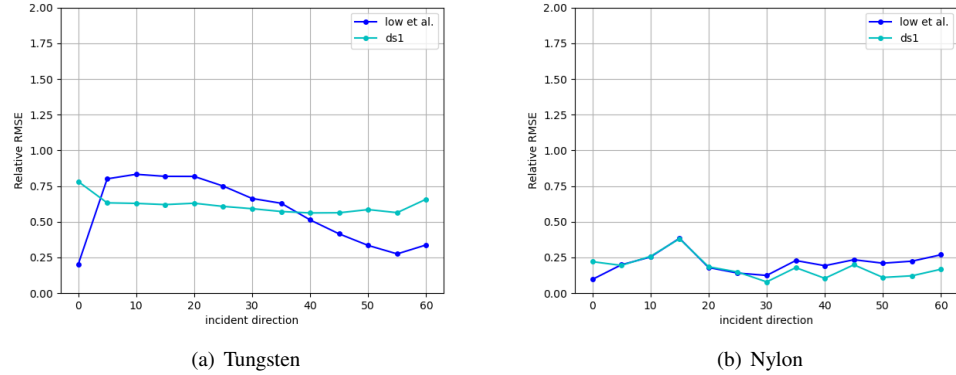


Fig. 8. Relative RMSE errors as a function of incident angle for two MERL materials. We note that our results (DS1) are comparable to the ones in [5].

238 4. Objective B: Spectral Simplification

239 The previous section was mainly targeted towards the use of inplane data for visual rendering.
 240 However, our measurements (unlike the MERL measurements designed for rendering) consists of
 241 31 wavelengths. Obtaining these measurements take considerable time. Our goal is to simplify
 242 the spectral measurements using an artificial neural network.

243 4.1. Prior Work

244 In one of the early works, [16], a learning-based solution is shown to generate the surface
 245 appearance. The method uses a single photograph and a self-supervised way of generating more
 246 data to model physically plausible spatially varying surface reflectance. This method limits the
 247 output to only a spatially varying albedo and homogeneous specular components. Using active
 248 lighting with a mobile phone flashlight, better [17, 18] specular effects were achieved. In all these
 249 cases, the learned neural network has fixed captured input, and thus the process generalizes the
 250 fitting to only this data and its produced output. Multiple captures are required for generating

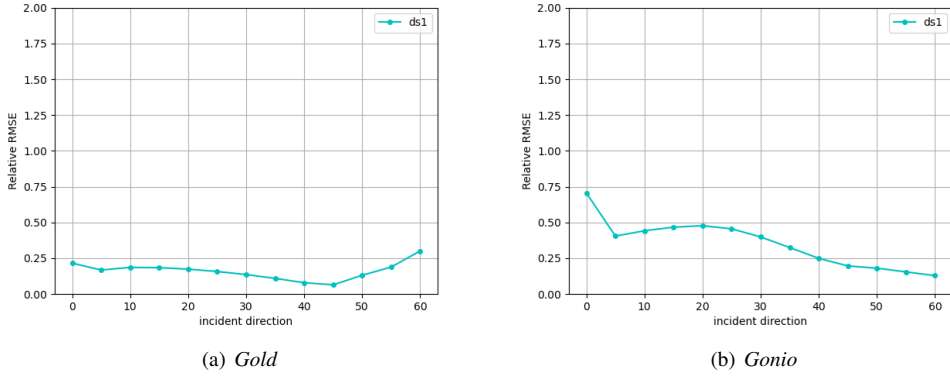


Fig. 9. Relative RMSE errors as a function of incident angle for GCMS data.

251 accurate reconstruction. To further improve the state-of-the-art, [7] takes an arbitrary number of
 252 inputs and generates a latent space explicitly, which can be taken to be similar to a parametric
 253 representation. This can then be subsequently used for generating complex appearances. A
 254 similar approach is adopted in DeepBRDF [19], which, however, explicitly uses the MERL
 255 database and BRDF measurements. These BRDF measurements are represented as images and
 256 fed to a convolutional neural network to obtain a latent representation, and for BRDF editing,
 257 are back converted to BRDF. This is based on the realistic image synthesis theory of light
 258 transport [20], albeit in the RGB domain. As mentioned earlier, the MERL database has isotropic
 259 materials.

260 Contrasting [19] is the work in [21], which also creates a latent representation that can be used
 261 further in rendering. The basic neural network (NBRDF) (in [21]) that creates a BRDF uses a
 262 small MLP. The anisotropic materials in [3] – albeit in the RGB domain – can also be modelled.

263 In all of the above cases, the emphasis has been in modeling and rendering, and working with
 264 tristimulus data.

265 Motivated by NBRDF [21], we propose an MLP. In contrast to NBRDF, however, we work
 266 in the (much larger than 3) spectral domain with the ultimate goal being the production of
 267 measurements, rather than BRDF editing or rendering.

268 4.2. MLP network

269 Given the complex optical properties of the packaging print materials *Gold* and *Gonio*, an MLP
 270 network was designed with three hidden layers and 10 nodes each². The BRDF values measured
 271 in Section 2.2 is used as training data to calculate the error signal when training the network.
 272 Table 2 shows the distribution of incident angles for training and testing. It was ensured that
 273 the incident directions covered in the training dataset were not encountered in the test set. The
 274 network takes the incident and reflected directions as an input, along with the spectral wavelength
 275 (400 – 700 nm), to predict the sample BRDF as an output.

276 The network was optimized using the exponential weighted Mean Squared Error (MSE) loss
 277 term given in Equation 6. These weights assign higher values in the specular region, pushing the

²Variations of this architecture were considered and the final choice was made based on model performance metrics (loss from Equation 6 for the test dataset in Table 2).

Dataset	Incident angles (θ_i°)
Test	$\{-50^\circ, -35^\circ, -20^\circ, -5^\circ, 10^\circ, 25^\circ, 40^\circ, 55^\circ\}$
Train	Angles at $5^\circ \in [-60^\circ, 60^\circ]$ excluding angles in Test

Table 2. Consideration of angles used to train the ANN.

278 network to capture the specular peaks accurately.

$$L_{MLP} = \frac{1}{N} \sum_{n=1}^N e^{-\gamma \cdot |\theta_i^\circ - \theta_r^\circ|} \cdot (f_{\text{mea}} - f_{\text{pred}})^2 \quad (6)$$

279 In Equation 6, f_{mea} is the measured sample BRDF, f_{pred} is the network output, γ is a hyperparameter
280 responsible for modulating the weight assigned to specular predictions, and θ_i and θ_r are the
281 incident and reflected directions in degree. An ADAM optimiser was used with an exponentially
282 decaying learning rate of 0.01. The MLP was trained for a total of 30 epochs, and the weights
283 with the best test accuracy were chosen. For γ , we experimentally determine the value of 3 to be
284 suitable for a general material with more specular ones requiring a higher value.

285 4.3. Objective B: Results

286 In this section, we show results for the BRDF plots and quantitative errors. Visual renderings are
287 not shown since the goal is to consider all possible measured wavelengths.

288 4.3.1. Visual Plots

289 We use the MLP network in the spectral domain to estimate the material BRDF. Figure 10 shows
290 the BRDF for the *Gold* sample for 7 wavelengths³ and for a single incident direction of -50° .
291 From the figure, we see that the network predicts the BRDF measurement data of the sample
292 reasonably accurately and can learn the underlying BRDF trends to extrapolate the unknown
293 BRDF measurement data. This learning is despite the fact that there are only 25 incident angles
294 to learn from.

295 4.3.2. Quantitative Errors

296 The network does oversimplify⁴ the BRDF in the specular regions due to the limited training data.
297 To analyze network performance across the spectrum, we provide (see Figure 11) box-and-whisker
298 plots similar to Section 3.3 for the relative rmse metric (Eq. 5). Naturally, we only consider
299 errors from the test data, not the training data. Here, for a specific wavelength and for a given
300 incident direction, all reflected directions are clubbed together to form a single data point. The
301 box-and-whisker plot thus shows the distribution of errors across multiple incident directions.
302 For the error computation, we consider (for each unseen incident angle), reflected angles in
303 the expected glossy region (i.e., where the incident angle approximately equals the angle of
304 reflection). In particular, we use a 1° interval for the reflected angle to closely examine the errors.
305 This is because we expect to see more errors in the glossy region.

306 Note that we also show the relevant value of the BRDF as a line plot. As an example, consider
307 wavelength 640nm for the *Gonio* sample. Our predicted value when the measured ground truth
308 expected value is 0.8 corresponds to $0.8 \pm 0.71 \times 0.8$, i.e., ≈ 0.85 which is a reasonable error
309 considering the experiments of [5]. For the *Gold* sample, picking a random angle of 500 nm we
310 see that the value of 0.7 could be predicted as $0.7 \pm 0.12 \times 0.7$, i.e., ≈ 0.7084 .

³We show 7 wavelengths across the spectrum only for visual clarity. Results for all wavelengths are in the supplementary material.

⁴We considered loss functions that are more forgiving to outliers (L1 loss) and weighing specular samples differently but the results were similar and provide marginal improvement.

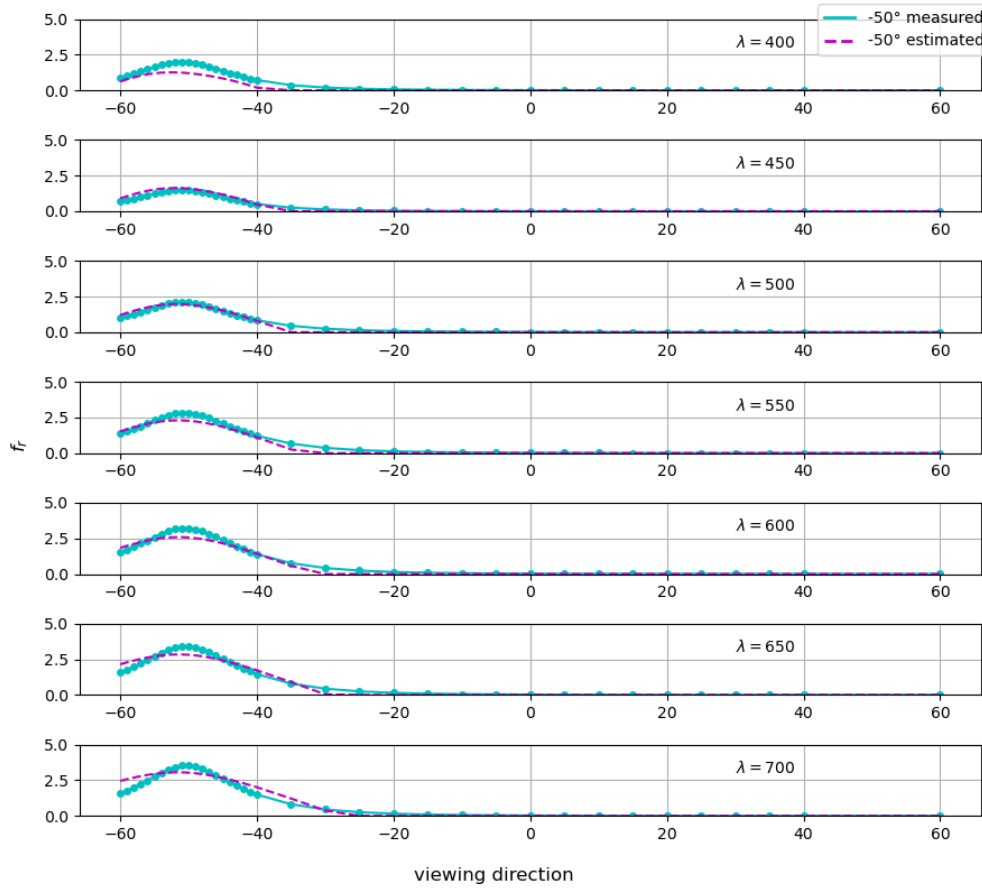


Fig. 10. Measured and predicted spectral BRDF for seven wavelengths of the *Gold* packaging sample.

311 4.4. Discussion

312 Although neural networks present an interesting approach to data approximation, their data-
 313 hungry nature limits their abilities. The strength that networks bring is more towards the offered
 314 flexibility. Nevertheless, our experiments indicate their feasibility.

315 Parametric models are built with very strong domain priors allowing them to learn the
 316 underlying physics with significantly fewer measurements compared to the neural networks.
 317 While parametric models are more efficient, they are limited by the accuracy of the underlying
 318 theory. There maybe limited applicability to a parametric model, and something like the ABC
 319 model we use in this study can not directly apply to a different range of materials (like anisotropic
 320 materials). Networks, however, can do a good job of abstracting the theory allowing one to use
 321 the same architecture on a wide spectrum of materials.

322 5. Conclusion

323 In-plane BRDF measurements of the packaging print materials were obtained using a commercially
 324 available goniospectrophotometer. Visual fidelity loss (due to a reduced dataset) via a parametric
 325 model was investigated using real-world packaging print materials and the MERL dataset

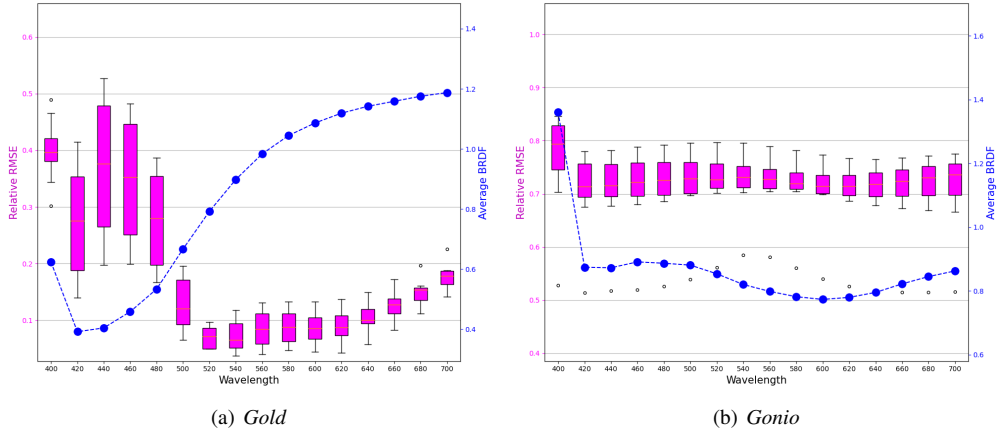


Fig. 11. Box-and-whisker plots showing relative RMSE for *Gold* (left) and *Gonio* (right) across wavelengths. Only test data (see Table 2) is used to calculate the error metric. The figure also shows the true measured value of the BRDF. As an example for *Gold*, the network could predict for $\lambda = 500\text{nm}$ the BRDF as 0.7084 instead of 0.7.

326 materials. An optimal set of reflectance model parameters for the packaging print materials,
 327 along with five MERL materials, were estimated using an in-plane BRDF measurement dataset.
 328 This paper demonstrates that in-plane measurements have relative RMSE errors comparable to
 329 the best known results for parameter fitting for the ABC model despite a large (256x) reduction
 330 in data. In ablation studies, the paper shows that a measurement dataset that is as small as six
 331 reflected directions for a single incident direction can be salient enough to successfully render
 332 the reflectance and characterize the optical properties of some isotropic materials.

333 With the spectral data being richer than its tristimulus counterpart and the existing analytical
 334 models being restricted to the RGB space, multi-layer perceptron networks were proposed for
 335 spectral BRDF estimation to reduce the acquisition process. These networks learn underlying
 336 patterns in the BRDF data and provide suitable approximates that we can use to our advantage
 337 and help reduce data acquisition times. The suggested approaches offer a significant reduction in
 338 the required measurement data and thus acquisition time.

339 All our conclusions are based on visual, and quantitative ablation studies.

340 Funding

341 The work presented in this paper did not receive funding from any funding agency in the public,
 342 commercial, or not-for-profit sectors.

343 References

- 344 1. F. E. Nicodemus, J. Richmond, J. J. Hsia, I. W. Ginsberg, and T. Limperis, “Geometrical considerations and
 345 nomenclature for reflectance,” Monograph 160, National Bureau of Standards (US) (1977).
- 346 2. K. Kehren, P. Urban, and E. Dörsam, “Bidirectional reflectance and texture database of printed special effect colors,”
 347 in *Color and Imaging Conference*, vol. 19 (Society of Imaging Science and Technology, 2011), pp. 316–321.
- 348 3. J. Dupuy and W. Jakob, “An adaptive parameterization for efficient material acquisition and rendering,” ACM
 349 Transactions on graphics (TOG) **37**, 1–14 (2018).
- 350 4. D. Guarnera, G. C. Guarnera, A. Ghosh, C. Denk, and M. Glencross, “Brdf representation and acquisition,” Comput.
 351 Graph. Forum **35**, 625–650 (2016).
- 352 5. J. Löw, J. Kronander, A. Ynnerman, and J. Unger, “Brdf models for accurate and efficient rendering of glossy
 353 surfaces,” ACM Transactions on Graph. (ToG) **31**, 9 (2012).
- 354 6. R. L. Cook and K. E. Torrance, “A reflectance model for computer graphics,” ACM Transactions on Graph. (ToG) **1**,
 355 7–24 (1982).

- 356 7. D. Gao, X. Li, Y. Dong, P. Peers, K. Xu, and X. Tong, “Deep inverse rendering for high-resolution svbrdf estimation
357 from an arbitrary number of images.” ACM Trans. Graph. **38**, 134–1 (2019).
- 358 8. J. Fan, B. Wang, M. Hasan, J. Yang, and L.-Q. Yan, “Neural layered brdfs,” in *ACM SIGGRAPH 2022 Conference
359 Proceedings*, (2022), pp. 1–8.
- 360 9. W. Matusik, H. Pfister, M. Brand, and L. McMillan, “A data-driven reflectance model,” ACM Transactions on Graph.
361 (TOG) **22**, 759–769 (2003).
- 362 10. K. Kehren, “Optical properties and visual appearance of printed special effect colors,” Ph.D. thesis, Technischen
363 Universität Darmstadt, Darmstadt, Germany (2013).
- 364 11. A. Sole, G. C. Guarnera, I. Farup, and P. Nussbaum, “Measurement and rendering of complex non-diffuse and
365 goniochromatic packaging materials,” The Vis. Comput. **37**, 2207–2220 (2021).
- 366 12. E. P. Lafortune, S.-C. Foo, K. E. Torrance, and D. P. Greenberg, “Non-linear approximation of reflectance functions,”
367 in *Proceedings of the 24th annual conference on Computer graphics and interactive techniques*, (1997), pp. 117–126.
- 368 13. C. IEC, “61966-2-1: 1999: Multimedia systems and equipment—colour measurement and management—part 2-1:
369 Colour management—default rgb colour space—srgb,” CIE: Vienna, Austria (1999).
- 370 14. A. Ngan, F. Durand, and W. Matusik, “Experimental analysis of brdf models.” Render. Tech. **2005**, 2 (2005).
- 371 15. W. Jakob, S. Speierer, N. Roussel, M. Nimier-David, D. Vicini, T. Zeltner, B. Nicolet, M. Crespo, V. Leroy, and
372 Z. Zhang, “Mitsuba renderer,” (2010).
- 373 16. X. Li, Y. Dong, P. Peers, and X. Tong, “Modeling surface appearance from a single photograph using self-augmented
374 convolutional neural networks,” ACM Transactions on Graph. (ToG) **36**, 1–11 (2017).
- 375 17. Z. Li, Z. Xu, R. Ramamoorthi, K. Sunkavalli, and M. Chandraker, “Learning to reconstruct shape and spatially-varying
376 reflectance from a single image,” ACM Transactions on Graph. (TOG) **37**, 1–11 (2018).
- 377 18. V. Deschaintre, M. Aittala, F. Durand, G. Drettakis, and A. Bousseau, “Single-image svbrdf capture with a
378 rendering-aware deep network,” ACM Transactions on Graph. (ToG) **37**, 1–15 (2018).
- 379 19. B. Hu, J. Guo, Y. Chen, M. Li, and Y. Guo, “Deepbrdf: A deep representation for manipulating measured brdf,” in
380 *Computer Graphics Forum*, vol. 39 (Wiley Online Library, 2020), pp. 157–166.
- 381 20. M. F. Cohen and J. R. Wallace, *Radiosity and realistic image synthesis* (Morgan Kaufmann, London, UK, 1993).
- 382 21. A. Sztrajman, G. Rainer, T. Ritschel, and T. Weyrich, “Neural brdf representation and importance sampling,” Comput.
383 Graph. Forum **40**, 332–346 (2021).
- 384 22. E. Kirchner and W. Cramer, “Making sense of measurement geometries for multi-angle spectrophotometers,” Color.
385 Res. & Appl. **37**, 186–198 (2012).
- 386 23. C. McCamy, “Observation and measurement of the appearance of metallic materials. part i. macro appearance,”
387 Color. Res. & Appl. **21**, 292–304 (1996).
- 388 24. J. Palmer and B. G. Grant, *The Art of Radiometry*, ISBN 978-0-8194-7245-8 (SPIE Press Bellingham, Washington
389 USA, 2010).

390 A. Appendix: Compact BRDF models

391 The “ABC” parametric model [5] defined in Equation 7 and used in this paper is based on the
392 well-established micro-facet Cook-Torrance model [6] that takes into account glossy surfaces and
393 is based on the Rayleigh-Rice light scattering theory and the micro-facet theory.

$$f(\mathbf{l}, \mathbf{v}) = \frac{k_d}{\pi} + \frac{F(\theta_h)G(\mathbf{n} \cdot \mathbf{l}, \mathbf{n} \cdot \mathbf{v})S(\sqrt{1 - (\mathbf{n} \cdot \mathbf{h})^2})}{(\mathbf{n} \cdot \mathbf{l})(\mathbf{n} \cdot \mathbf{v})} \quad (7)$$

394 In Equation 7, θ_h is the half angle between the surface normal \mathbf{n} and the halfway vector \mathbf{h} . k_d is
395 a presumed diffuse component parameter, F the Fresnel factor [6] (as defined in Equation 8), and
396 G is the geometrical attenuation factor (as defined in Equation 9).

$$F = \frac{(g - c)^2}{2(g + c)^2} \left\{ 1 + \frac{[c(g + c) - 1]^2}{[c(g - c) + 1]^2} \right\} \quad (8)$$

$$G = \min \left\{ 1, \frac{2(\mathbf{n} \cdot \mathbf{h})(\mathbf{n} \cdot \mathbf{v})}{(\mathbf{v} \cdot \mathbf{h})}, \frac{2(\mathbf{n} \cdot \mathbf{h})(\mathbf{n} \cdot \mathbf{l})}{(\mathbf{v} \cdot \mathbf{h})} \right\} \quad (9)$$

397 398 In Equation (8), $c = \mathbf{v} \cdot \mathbf{h}$, $g = \eta^2 + c^2 - 1$ and η is the index of refraction. Finally, S is the
399 ABC-based micro-facet distribution given in Equation (10).

$$S(f) = \frac{A}{(1 + Bf^2)^C}, \quad (10)$$

400 In Equation (10), B and C define the width of the specular peaks and the fall-off rate of wide-angle
 401 scattering, and A is the specular component parameter.

402 **B. Reflectance factor**

403 The BRDF can be theoretically infinite and therefore, commercially available multi-angle
 404 spectrophotometers and goniospectrophotometers [22, 23] measure the *biconical reflectance* [20],
 405 or simply the reflectance which is the ratio of the reflected to incident flux. Mathematically, with
 406 θ_r representing the reflected angle and ω_r representing the reflected solid angle, the reflectance is

$$\beta(2\pi \rightarrow 2\pi) = \frac{\int_{\Omega_r} L_r(\mathbf{v}) \cos \theta_r d\omega_r}{\int_{\Omega_i} L_i(\mathbf{l}) \cos \theta_i d\omega_i} \quad (11)$$

407 Devices may not output the BRDF or the reflectance per se since they are calibrated with respect
 408 to a theoretically perfect reflecting diffuse (PRD) surface. The BRDF is therefore obtained from
 409 the ratio relation of the measured values

$$\frac{f_{\text{material}}}{f_{\text{PRD}}} = \frac{\beta_{\text{material}}}{\beta_{\text{PRD}}} \quad (12)$$

410 with the BRDF of a PRD being $\frac{1}{\pi}$. However, in the absence of the theoretical PRD, one can use
 411 another surface such as the Munsell white N9 sheet which has a reflectivity of 78.66% [24].
 412 Thus we calculate the bidirectional reflectance at the material surface using Equation (13)

$$f \approx \frac{0.79}{\pi} \frac{\beta_{\text{material}}}{\beta_{\text{Munsell}}} \quad (13)$$

413 where the numerator is the value output by the measurement instrument (GCMS in our case).
 414 Once the BRDF is known, the related photometric quantities such as the radiance L_r or the flux
 415 can be calculated.

416 **C. Appendix: Ablation Studies**

417 In Section 3.3 we showed that relatively small in-plane measurements are sufficient for visual
 418 rendering. A natural question to ask is, “Can we further reduce the data necessary for generating
 419 visually accurate renderings?” To test this, we reduce our data as per the strategies noted in
 Table 3 and Table 4.

Dataset	θ_i interval	θ_r interval: Diffuse	θ_r interval: Glossy
DS1	5°	5°	1°
DS2	15°	10°	2°
DS3	30°	20°	3°

Table 3. Angle intervals for performing ablation studies with reduced fitting data (DS2–DS3). Similar to Table 1, incident and reflected angles are between -60° and 60°.

420

421 *C.1. MERL data*

422 Following the convention in Section 3.3, we provide three sets of results for the reduced datasets.

- 423 1. We use parameters estimated from reduced datasets to render a 3D scene as shown in
 424 Figure 12.

Dataset	Incident angle (θ_i°)	Reflected angle (θ_r°)
DS4	30°	-60°, -20°, 20°, 28°, 36°, 60°

Table 4. Incident and reflected angles for the DS4 reduced dataset. Only **six** measurements are used.



Fig. 12. Scene renderings for visual comparison between parameters obtained with reduced in-plane datasets (DS1-DS4) on MERL materials. NY, and TC are Nylon, and Tungsten Carbide, respectively.

- 425 2. We also plot BRDF values for the MERL materials estimated from the reduced in-plane
 426 datasets in Figure 13. As before, the full set of in-plane measurements (DS1) has a total of
 427 900 measurements (roughly 35-36 measurements for 25 incident angles), as opposed to
 428 the 256x more samples used by Low et al [5].

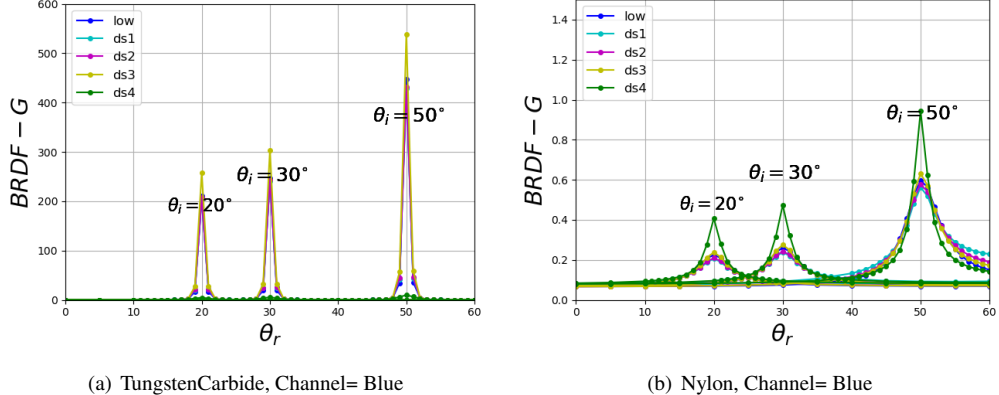


Fig. 13. Parametrically calculated BRDF of MERL materials across reflected directions.

429 We observe that the quality of our fits and the renderings degrade around Dataset 3 or 4,
 430 depending on material complexity. The supplementary results has the complete data for
 431 all channels (and offer no new insights, generally speaking, except to provide actual values
 432 for repeatability purposes).

- 433 3. Finally, to better understand the error distribution across datasets, in Figure 14, we provide
 434 box-and-whisker plots for the relative-rmse metric as in Equation 5. Here each datapoint

435 corresponds to a particular incident direction. We observe that Datasets 3 and 4 have more
 436 variance, but values, as expected, depend on the material.

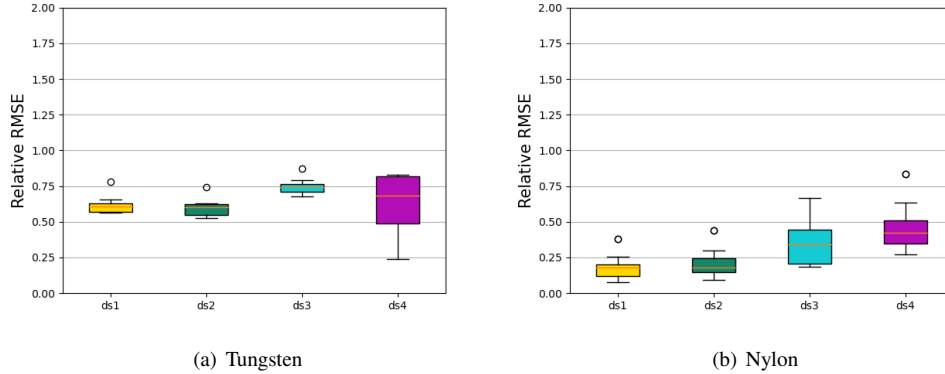


Fig. 14. Box-and-whisker plots showing relative RMSE calculated using Equation 5 for the MERL materials TungstenCarbide and Nylon. The orange line in the box shows the median error obtained for the measurement datasets.

437 C.2. GCMS data

438 Similar plots and renderings are also captured for the packaging print materials (shown in
 439 Figure 16 and Figure 17) measured using the GCMS. Box-and-whisker plots in Figure 15 show
 440 the effects of reducing data on the relative error.

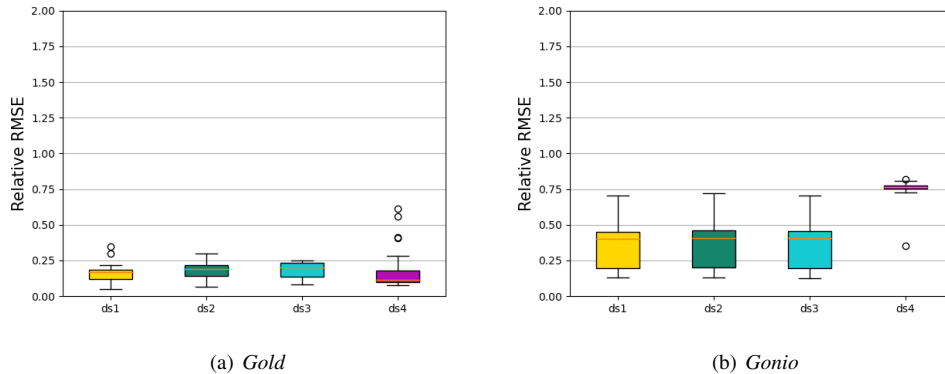


Fig. 15. Box-and-whisker plots showing relative RMSE calculated using Equation 5 for the packaging print materials *Gold* and *Gonio*. The orange line in the box shows the median error obtained for the measurement datasets (refer Table 3 for datasets used).

441 C.3. Commentary: Objective A

442 From Figure 13 datasets DS2 and DS3 show a fit that is comparable with the full (in-plane)
 443 measurement dataset (DS1). This can be confirmed from the relative error calculated and shown

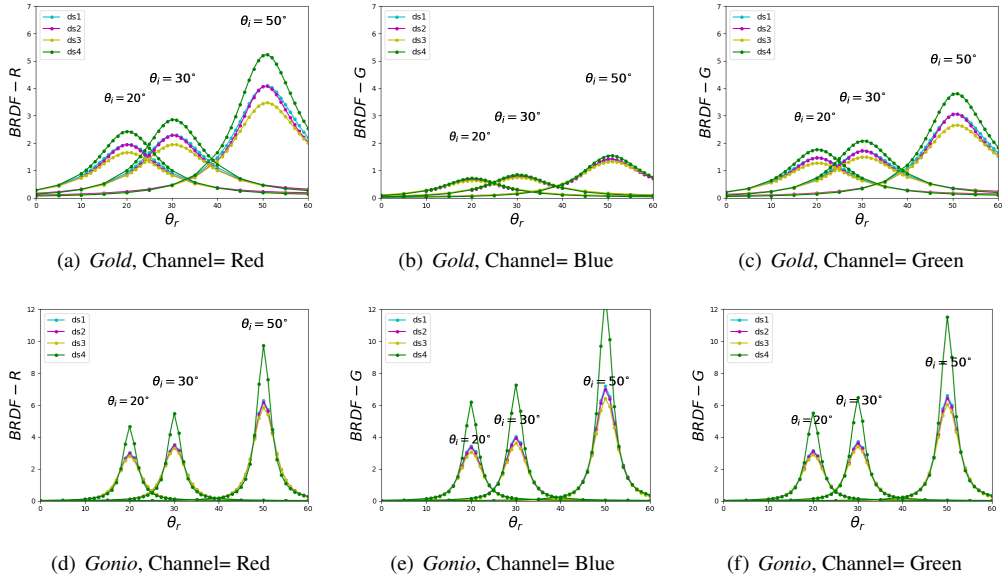


Fig. 16. Parametrically calculated BRDF of our measured materials. Values across reflected directions for the three channels. Refer Table 3 for incident and reflected angles corresponding to each dataset.

in Figure 14. From the renderings in Figure 12, the difference across datasets is indistinguishable (even in the specular region).

For the packaging print materials, the specular reflectance peak being at a much lower value along with a higher full-width half maximum value compared to the MERL materials used, the ABC model seems to perform better for the same datasets (DS1 – DS4). Evaluating the packaging print material renderings (Figure 17) it is observed that a dataset as small as the DS4 dataset (six measurements) can be enough to visualize the reflectance and characterize its optical properties for such isotropic materials.

However, we can see that the ABC model estimated using the DS4 dataset (unlike other datasets) fits poorly for the MERL dataset, especially for non-diffuse materials. This dataset seems to be not enough for the highly specular MERL materials (like the *TungstenCarbide*) due to the limited fitting data in the specular reflected directions. A similar trend is observed for the *Gonio* print material (Figure 16).

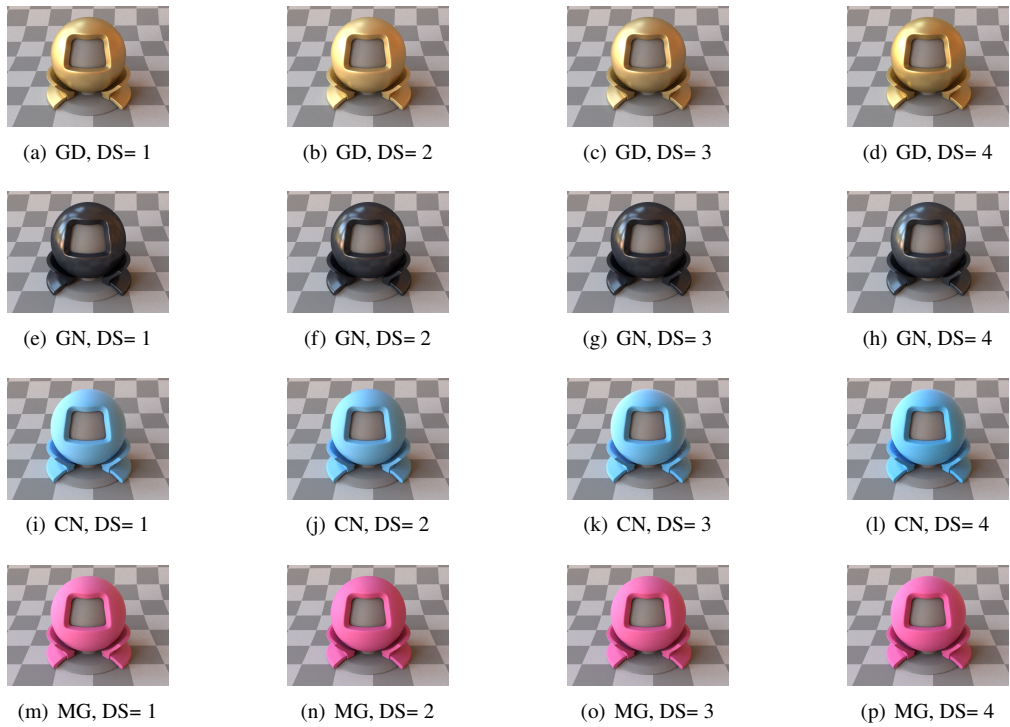


Fig. 17. Scene renderings for visual comparison between parameters obtained for different in-plane datasets on our measured materials. Refer Table 3 and Table 4 for the datasets DS={1,2,3,4}. GD, GN, CN, and MG are *Gold*, *Gonio*, *CN*, and *MaG*, respectively.